Atomization and Sprays, 21 (12): 1009–1031 (2011)

STEADY AND TRANSIENT DROPLET DISPERSION IN AN AIR-ASSIST INTERNALLY MIXING CONE ATOMIZER

Amir A. Aliabadi, Kelly W. J. Lim, Steven N. Rogak, & Sheldon I. Green

Department of Mechanical Engineering, University of British Columbia, 3321—2260 West Mall, Vancouver, British Columbia, V6T 1Z4, Canada

*Address all correspondence to E-mail: aliabadi@interchange.ubc.ca

Original Manuscript Submitted: 12/6/2011; Final Draft Received: 4/30/2012

Droplet dispersion for steady and transient sprays produced by an air-assist internally mixing cone atomizer is studied using high-speed laser imaging, shadowgraphy, and particle tracking velocimetry (PTV). For this spray, large droplets form close to the periphery while small droplets form close to the centerline. Radial dispersion of droplets is a function of droplet relaxation time and fluctuating flow characteristic times so that small droplets disperse more effectively in the radial direction than large droplets due to turbulent diffusion. For the transient spray, the overall axial and radial penetration of the spray is self-preserving and similar to penetration of starting continuous phase jets. Axial dispersion of droplets is a function of droplet relaxation time and the mean flow characteristic time. The leading edge of the spray exhibits higher turbulence than the trailing edge, which is characterized by very large eddies and smaller Reynolds numbers. The dispersion behavior at far-field away from the breakup region is expected to be similar for many dilute air-assist, internally mixing round sprays.

KEY WORDS: *air-assist, internally mixing, spray, atomizer, droplet, dispersion, starting jet, imaging, shadowgraphy, particle tracking velocimetry (PTV)*

1. INTRODUCTION

1.1 Droplet Dispersion in Steady Air-Assist Atomizers

Droplet dispersion from air-assist atomizers in axial x and radial r directions may be a function of many parameters. These include the type (e.g., internal versus external mixing) and geometry (exit diameters for liquid and gas streams) of the air-assist atomizer, droplet diameter d, the gas to liquid mass loading ratio $\dot{m}_g/\dot{m}_l$, the gas to liquid momentum loading ratio p_g/p_l, the gas Weber number We_g, the gas and liquid Reynolds numbers Re_g and Re_l, droplet evaporation rate, gravitational effects, and the spray breakup structure. This study considers the effects of droplet diameter, gas and liquid Reynolds numbers, Weber number, and mass loading ratio.

The overall shape of a round air-assist spray can be characterized using the penetration, cone angle, and equivalent spray angle (Rizkalla and Lefebvre, 1975); however, none of these measurements provide any information regarding the droplet size within the spray. Instead, some studies report droplet size in a spray using Sauter mean diameter (SMD) or d_{32}, the overall volume-to-surface ratio. Eroglu and Chigier

1044–5110/11/$35.00

NOMENCLATURE

A_g	nozzle gas exit area
A_l	nozzle liquid exit area
ALR	air-to-liquid mass ratio
B	spray self-similarity constant
C	semi empirical coefficient for $k-\epsilon$ turbulence models
C_r	jet radial dispersion self-preserving constant
C_x	jet axial dispersion self-preserving constant
d	droplet diameter
d_{10}	number mean diameter
d_{32}	volume to surface area ratio or Sauter mean diameter (SMD)
d_g	nozzle gas exit diameter
d_l	nozzle liquid exit diameter
k	turbulent kinetic energy
L	characteristic flow length
$\dot{m}_g$	gas mass flow rate
$\dot{m}_l$	liquid mass flow rate
N	number of measurements
n	continuous phase jet or spray axial dispersion self-preserving constant
N_f	number fraction
P	pressure, P value for statistical analysis
p_g	nozzle gas exit momentum
p_l	nozzle liquid exit momentum
Pe_L	Lagrangian Péclet number
PTV	particle tracking velocimetry
r	radial distance from nozzle
R^2	coefficient of determination
Re_g	gas Reynolds number
Re_l	liquid Reynolds number
St_k	Kolmogorov-Stokes number
St_m	mean Stokes number
St_t	turbulent Stokes number
SMD	Sauter mean diameter
t	time, t statistic
t_d	imaging time delay
t_f	time delay to reach maximum liquid/gas flow
t_0	time delay
t^*	nondimensional time
U	axial droplet velocity
U_c	axial droplet velocity in the center of spray
U_g	nozzle gas exit velocity
U_l	nozzle liquid exit velocity
U_r	relative velocity between liquid and gas
V_f	volume fraction
v_t	terminal droplet velocity
We_g	aerodynamic Weber number
x	axial distance from nozzle, random variable
x_0	axial distance of virtual origin from nozzle
$\overline{x}$	mean value statistic

Greek Symbols

ϵ	turbulent dissipation rate, droplet diffusivity
μ_g	gas dynamic viscosity
μ_l	liquid dynamic viscosity
ν	degrees of freedom
ν_g	gas kinematic viscosity
ν_l	liquid kinematic viscosity
ρ_g	gas density
ρ_l	liquid density
σ	liquid surface tension, standard deviation
τ_d	droplet relaxation time
τ_g	characteristic mean flow time scale
τ_e	characteristic eddy time scale
τ_k	characteristic Kolmogorov time scale

(1991), Hardalupas and Whitelaw (1994), and Karl et al. (1996) performed measurements of d_{32} as a function of axial and radial distances for externally mixing air-assist atomizers. Karl et al. (1996) found that d_{32} increases at the spray periphery due to the greater momentum of larger droplets and their ability to migrate to the side given the initial velocity in the radial direction. Hardalupas and Whitelaw (1994) found a decreasing d_{32} versus radial distance. To the contrary, given different operating liquid and gas pressures, Eroglu and Chigier (1991) found that d_{32} could rise, fall, or stay the same with increasing radial

distance. These studies did not report a major shift in the value of d_{32} as a function of axial distance for steady sprays.

Empirical correlations of d_{32} have been developed for air-assist atomizers (Rizk and Lefebvre, 1984; Rizkalla and Lefebvre, 1975; Sakai et al., 1978). Rizkalla and Lefebvre (1975) developed the following correlation for d_{32} for an internally mixing atomizer:

$$d_{32} = 0.95\frac{(\sigma\dot{m}_l)^{0.33}}{U_r\rho_l^{0.37}\rho_g^{0.30}}\left(1+\frac{1}{\mathrm{ALR}}\right)^{1.70} + 0.13\left(\frac{\mu_l^2 d_g}{\sigma\rho_l}\right)^{0.5}\left(1+\frac{1}{\mathrm{ALR}}\right)^{1.70} \quad (1)$$

where ALR is the air-to-liquid mass ratio $\dot{m}_g/\dot{m}_l$ and U_r is the relative velocity between air and liquid. Water, kerosene, and other fluids were employed in these tests. The air velocity was held in the range 70–125 m/s. ALR was in the range 3–9. Experiments were run at room and elevated temperatures. This correlation is accurate within 8% over a broad range of air and liquid properties that include our operating conditions for nitrogen and water.

Size-resolved droplet concentration and velocity within a spray also describe the dispersion behavior. Eroglu and Chigier (1991), Hardalupas and Whitelaw (1994), Karl et al. (1996), and de Vega et al. (2000) performed measurements of droplet concentration and mean velocity as a function of axial and radial distances for steady, externally mixing air-assist atomizers. Nijdam et al. (2008) provided comparable measurements for an internally mixing air-assist atomizer. Also, Kennedy and Moody (1998) performed velocity and radial dispersion measurements of monodisperse droplets in a steady gas jet as a function of gas Reynolds number and position. It was found that total concentration at large axial distances follows a self-similar Gaussian distribution versus non-dimensional radial distance (de Vega et al., 2000; Karl et al., 1996). Also, it was found that nondimensional axial velocity profiles are self-similar and appear as Gaussian when plotted against nondimensional radial distance (Arcoumanis and Gavaises, 1998; de Vega et al., 2000; Hussein et al., 1994; Karl et al., 1996; Kennedy and Moody, 1998; Li et al., 2009). de Vega et al. (2000) and Nijdam et al. (2008) verified that smaller droplets have higher turbulent intensities in sprays, both axially and radially. Kennedy and Moody (1998) verified, experimentally, that smaller droplets disperse more effectively in the radial direction. These studies hint that, in a full-size distribution, smaller droplets diffuse more quickly in the radial direction, but the validity of this statement in the context of air-assist atomization using liquid breakup is yet to be confirmed.

Axial deceleration of continuous phase jets and sprays is an important measure for droplet dispersion in sprays. Gases and particle-laden jets are characterized by a decreasing centerline axial mean velocity (deceleration) U_c as a function of axial distance x, upstream gas velocity U_g, virtual origin x_0, nozzle gas exit diameter d_g, and a constant B, in such a way that

$$\frac{U_g}{U_c} = \frac{1}{B}\left(\frac{x}{d_g} - \frac{x_0}{d_g}\right) \quad (2)$$

The values of B and x_0 vary among continuous phase jets, particle-laden jets, and sprays. For continuous phase jets, Hussein et al. (1994) gave $B \simeq 6$ and $x_0 \simeq 3d_g$; for particle-laden flows with low mass loadings, Hardalupas et al. (1989) gave $B \simeq 7.2$ and $x_0 \simeq 3.5d_g$; and for sprays, de Vega et al. (2000) gave $B \simeq 10$ and $x_0 \simeq -15d_g$. de Vega et al. (2000) found a faster deceleration for smaller droplets. Droplet mean axial velocity is dependent on droplet size and gas axial velocity, both of which must be measured accurately to describe the axial dispersion behavior.

Proper understanding of droplet dispersion in air-assist atomization requires knowledge of continuous phase (gas) jets. First, dispersion of fine droplets in dilute sprays can be approximated by that of gas jets, since fine droplets behave like fluid elements. Second, spray dispersion results from the interaction of droplets with the gas mean and turbulent flow components. The work of Sangras et al. (2002) and others (Kouros et al., 1993; Lahbabi et al., 1993; Rizk, 1958; Witze, 1983) allows comparison between dilute air-assist spray penetration and the penetration of continuous phase puffs, starting jets, and jets. The work of

Hussein et al. (1994) can be used to provide estimates for velocity distribution, kinetic energy, and dissipation rate in high-Reynolds-number axisymmetric turbulent jets, and subsequently, dilute sprays.

Droplet dispersion follows from the breakup processes that occur during the early stages of atomization (Engelbert et al., 1995; Lasheras et al., 1998; Varga et al., 2003). Shi and Kleinstreuer (2007) classify different breakup regimes for coaxial air-assist atomizers. The first step, called primary breakup, is due to the formation of ligaments and other irregular liquid elements along the surface of the liquid column. These irregular shapes break into large droplets. The droplets then undergo different forms of breakup, called secondary breakup, that includes "bag," "stripping," and "catastrophic" mechanisms.

The physics that govern primary and secondary breakup mechanisms are different (Lasheras et al., 1998). For small Weber numbers ($\mathrm{We}_g < 110$) surface tension dominates the droplet formation. For larger Weber numbers ($\mathrm{We}_g > 100$) fiber-type ligaments begin to form and they break into droplets by the Rayleigh-type capillary breakup mechanism. The intact liquid core in air-assist atomizers further persists downstream to a distance correlated to the gas-to-liquid momentum ratio. The smaller this ratio, the further the liquid stream travels before breakup. The secondary breakup of droplets results from the relative velocity between the droplet and the mean motion of the gas (slip velocity) or from the turbulence of the carrier gas. The former breakup process is termed "shear breakup" and the latter process is termed "turbulent breakup."

Lasheras et al. (1998) attribute the accumulation of larger droplets on the periphery of the spray due to different breakup regimes. The primary breakup is more dominant near the edge of the spray where shear forces are maximum at the gas-liquid interface. This mechanism is responsible for large droplet formation. On the other hand, the secondary breakup mechanisms (pressure and viscous forces by turbulent motion) are dominant at the center of the spray. These forces are responsible for smaller droplet formation. The radial profiles of d_{32} reduce in slope at larger axial distances, since fine droplets migrate to the periphery faster than large droplets. Explanation of droplet dispersion in an air-assist atomizer requires an understanding of primary and secondary breakup regimes in the spray.

The evaporation rate can significantly affect droplet dispersion if droplets are small and their evaporation time is comparable to their lifetime. For example, at 20% relative humidity, 1 μm droplets evaporate in 1 ms, 5 μm droplets evaporate in 35 ms, and 100 μm droplets evaporate in 10 s (Morawska, 2006). To reduce the effect of evaporation on size and dispersion measurements, it is desirable to analyze droplets for which the evaporation time is at least an order of magnitude larger than maximum time of flight. This will be the case for this study and will be explained in detail in Section 2.6.

Wells and Stock (1983) investigated the effect of body forces such as gravity on the dispersion of droplets in turbulent flows. They claimed that the impact of gravity will be negligible if the droplet terminal velocity v_t is less than the root mean square of fluid fluctuating velocity, which is the case for this study. Otherwise, gravitational and other body forces must be considered.

A droplet of diameter d, density ρ_l, suspended in a gas with dynamic viscosity μ_g, interacts with the mean and turbulent components of the gas flow. The droplet response in the flow can be understood by comparing the droplet relaxation time $\tau_d = \rho_l d^2/(18\mu_g)$ with other time scales in the flow. These time scales are the mean flow time scale $\tau_g = x/U_g$, the Kolmogorov time scale $\tau_k = \sqrt{\nu_g/\epsilon}$, and the characteristic eddy time scale $\tau_e = Ck/(\sqrt{2/3}\epsilon)$. The turbulent dissipation rate ϵ, kinetic energy k, and constant C can be estimated by those of gas jets in the case of dilute sprays (Kennedy and Moody, 1998). The Stokes number nondimensionalizes the droplet relaxation time using these flow time scales. Table 1 demonstrates possible Stokes numbers for spray dispersion.

Radial dispersion of droplets in air-assist atomizers can be quantified using droplet diffusivity and nondimensionalized using the convective time scale of the gas flow to yield a Lagrangian Péclet number (Kennedy and Moody, 1998). Droplet diffusivity

TABLE 1: Stokes numbers in spray droplet dispersion

Stokes number	Symbol	Definition
Mean Stokes number	St_m	τ_d/τ_g
Kolmogorov-Stokes number	St_k	τ_d/τ_k
Turbulent Stokes number	St_t	τ_d/τ_e

$\epsilon(d)$ and Lagrangian Péclet number $\mathrm{Pe}_L(d)$ are defined as

$$\epsilon(d) = \frac{1}{2}\frac{d}{dt} < r(d,t)r(d,t) > \tag{3}$$

$$\mathrm{Pe}_L(d) = \frac{U_g d_g}{\epsilon(d)} \tag{4}$$

This Péclet number can be calculated either locally or as an average over a distance.

1.2 Droplet Dispersion in Transient Air-Assist Atomizers

Droplet dispersion is less studied for transient air-assist atomizers. Most studies in the literature concerning transient sprays relate to liquid jets in engine fuel injectors (e.g., diesel engines). Arcoumanis and Gavaises (1998) have studied atomization from diesel injectors. They report decreasing d_{32} as a function of time at larger axial distances. They also performed velocimetry measurements as a function of time and position. Their study, however, did not provide detailed dispersion and velocimetry results for a complete droplet size distribution.

The overall transient dispersion of droplets in a round air-assist spray can be characterized in a similar way to those of continuous phase starting jets. Sangras et al. (2002) have shown that downstream of a continuous puff or starting jet, the flow evolves into a self-preserving structure such that dimensionless axial penetration $(x - x_0)/d_g$ is correlated with dimensionless time $(t - t_f)U_g/d_g$, and the dimensionless radial penetration $r/(x - x_0)$ is correlated with dimensionless axial penetration. These correlations are provided by

$$\frac{x - x_0}{d_g} = C_x \left(\frac{(t - t_f)U_g}{d_g} \right)^n \tag{5}$$

$$\frac{r}{x - x_0} = C_r \tag{6}$$

where C_x, C_r, and n are constants. n is usually 0.5 for starting jets and 0.25 for puffs. t_f is the time delay for the injected phase to reach its maximum flow rate (Sangras et al., 2002). It is speculated that the same correlation will explain the overall dispersion for dilute air-assist sprays with very fine droplets.

1.3 Objectives

Many studies only report dispersion properties for steady operation of air-assist atomizers. Even still, most studies primarily focus on single or mean droplet size dispersion characteristics while neglecting the effect of droplet breakup mechanisms in dispersion further downstream of sprays. In our study, the droplet dispersion characteristics for a cone air-assist, internally mixing nozzle is sought under both steady and transient operation modes, including spatially resolved size distributions for droplets.

The first part of this study focuses on steady spray dispersion behavior for an air-assist, internally mixing cone atomizer. The specific research objectives for this part are: (1) determine the effect of droplet breakup in the dispersion of droplets downstream of the spray; (2) determine the relationship between droplet size and radial dispersion with a focus on the size distribution of droplets. The second part extends the measurements to transient sprays. Specific objectives of this part are: (1) determine the self-preserving dispersion of the overall transient spray and compare it to that of transient continuous phase starting jets; (2) determine the droplet size distribution, Sauter mean diameter, and concentration for the leading and trailing edges of the transient spray as a function of time and the axial distance from the atomizer, and compare these with steady sprays; (3)

determine the velocity distribution as a function of axial distance and droplet size in the leading and trailing edges of the transient spray, and compare it with steady sprays; (4) explain the behavior of droplet dispersion and velocity using mean, Kolmogorov and turbulent Stokes numbers.

2. EXPERIMENTAL METHODS

The atomizer used in this study consists of an air nozzle assembly, two separate valves driven by a solenoid, a relay, a liquid tank, a pressure regulator, and two supply pressure lines. The nozzle assembly traverses in the horizontal x and vertical r directions. The gas and liquid lines are pressurized and the solenoid valves are operated by the relay. Two simultaneous pulses are supplied to the relay that powers the solenoids. This actuates the valves and allows liquid and pressurized gas to flow and create the spray.

The nozzle (SUQR-220B) was manufactured by Spraying Systems Co. with an orifice output diameter of $d_g = 2.4$ mm and an internal liquid jet diameter of $d_l = 1$ mm. The fluid mixing is shown in Fig. 1. The Liquid cap has the center orifice that carries the liquid into the air cap. Around the fluid cap, near the front gasket, there are four orifices that introduce the atomizing air into the liquid stream. The full nozzle assembly is shown in Fig. 2. Deionized water was used as liquid and pressurized nitrogen was used as gas for the spray tests. The temperature and relative humidity in the laboratory were 22–24°C and 45–55%, respectively.

2.1 Spray Penetration Test Setup

A "forward lighting" arrangement was used to take images of the spray using a LaVision Imager Intense Camera. A continuous light source was used so that a powerful backscattered signal from the droplets could be recorded. The physical distance between the camera and the atomizer was 2.7 m. A 50 mm 1:1.2 Nikon lens (386671) was used to provide a wide field of view of 475 mm. The area behind the atomizer was covered by a black mat. The camera exposure time was set to 500 μs. A complete schematic for the spray penetration test is shown in Fig. 3.

The atomizer and imaging were timed using a LabView system (consisting of a computer and a Na-

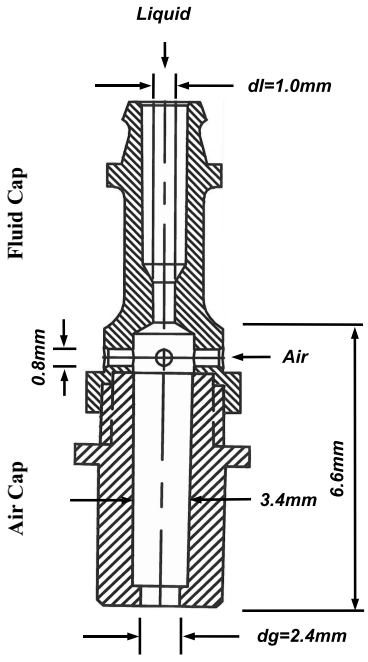

FIG. 1: Fluid mixing schematic.

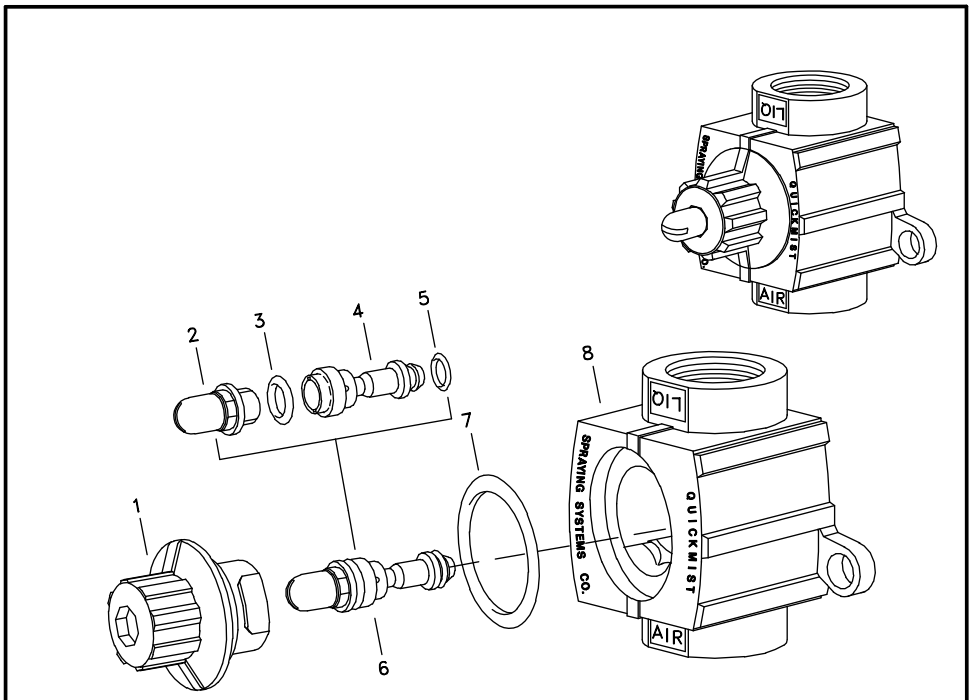

ITEM	PART NO.	DESCRIPTION
1	CP38862-KY	RETAINER CAP, KYNAR (GRAY)
2	PAQ*	AIR CAP, KYNAR
3	CP7717-2/11-VI	O'RING, VITON®
4	PFQ*	FLUID CAP, KYNAR
5	CP7717-3-VI	O'RING, VITON®
6	SUQ**	SPRAY SET-UP (INCLUDES ITEMS 2 THRU 5)
7	CP7717-2/117-VI	O'RING, VITON®
8	CP38867-1-KY	BODY, KYNAR (BLACK) FOR MODEL 1/4QMJML
	CPB38867-1-KY	BODY, KYNAR (BLACK) FOR MODEL B1/4QMJML
1/4QMJML QUICKMIST™ AIR ATOMIZING NOZZLE, KYNAR [1/4" NPT (F) INLET CONN.]		
B1/4QMJML QUICKMIST™ AIR ATOMIZING NOZZLE, KYNAR [1/4" BSPT (F) INLET CONN.]		

*SPECIFY AIR & FLUID CAP SIZES
**SPECIFY SPRAY SET-UP

DESCRIPTION:
1/4QMJML & B1/4QMJML
QUICKMIST
AIR ATOMIZING NOZZLES
WITH MOUNTING LUGS

Spraying Systems Co.®
Spray Nozzles and Accessories
P.O. Box 7900 - Wheaton, Il. 60189-7900

Rev. No.	Parts List No.
Ref.	PL 1/4QMJML & B1/4QMJML
	SHEET OF

FIG. 2: Nozzle assembly (courtesy of Spraying Systems Co.).

tional Instruments BNC-2121 pulse generator) and a LaVision system (consisting of a computer and a programmable timing unit (PTU) board to trigger the camera). First, a pulse was generated by the Lab-

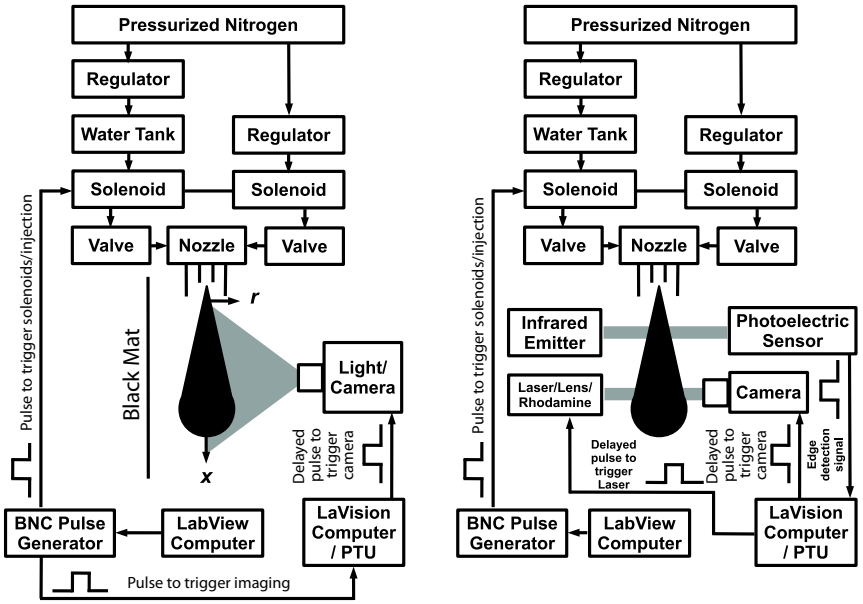

FIG. 3: Schematic for spray penetration (left) and shadowgraphy/PVT (right) test systems.

View system to trigger the solenoids and therefore initiated the injection. The same pulse was supplied to the LaVision system. Then the LaVision Sizemaster/Davis 7.2 program signaled the camera for imaging by a pulse that was delayed by various values so that penetration of the spray could be observed at different times after valve opening. This delay time ranged logarithmically from 10 ms to 40 ms in 20 steps. Two flow conditions were considered in this study (Table 2). The time resolution for the PTU sequencer I/O was 10 ns. The typical jitter between all outputs was less than 1 ns.

2.2 Spray Shadowgraphy Test Setup

A shadowgraphy technique was used to take close-up images of individual droplets. A "backlighting" arrangement was used to take images of the spray us-

TABLE 2: Flow conditions for the spray tests

Test	**1**	**2**
Nitrogen Pressure [psi]	30	50
Water Pressure [psi]	15	25
U_g [m/s]	[237][1]	[351]
U_l [m/s]	[0.37]	[0.25]
$\mathrm{Re}_g = U_g d_g/\nu_g$	34,600	51,200
$\mathrm{Re}_l = U_l d_l/\nu_l$	370	260
$\mathrm{We}_g = \rho_g(U_g - U_l)^2 d_l/\sigma$	940	2070
$\dot{m}_g/\dot{m}_l = (\rho_g A_g U_g)/(\rho_l A_l U_l)$	1.23	0.60
$p_g/p_l = (\rho_g A_g U_g^2)/(\rho_l A_l U_l^2)$	830	830

[1][] Velocities are estimated using gas and liquid flow rates, exit diameters, and densities at room temperature provided by the manufacturer

ing the LaVision Imager Intense camera. A pulsed laser (Big Sky Ultra) was used as a light source to shine a diverged beam of green light (532 nm) on a diffuse and fluorescent medium (liquid rhodamine). The collimated laser beam was passed through a lens so that the beam was traced as a round circle of about 2 cm in diameter on a flat container of liquid rhodamine. The physical distance between the camera and the atomized spray was about 10 cm. A $14X$ magnification Navitar lens was used to provide a narrow field of view of about 0.5×0.3 mm. The camera exposure time was set to 500 μs and the laser light source was fired at the end of the exposure time by the PTU unit. The actual exposure was just under 10 ns (the pulse width of the laser). Only test 1 flow conditions in Section 2.1 were used. It was desired to measure the droplet size distribution at a location at a known elapsed time after the spray injection. To obtain precise elapsed times, the valve actuation time variability must be eliminated. A pair of photoelectric sensors and an infrared emitter were arranged in a "through-beam" setup at the exit of the spray near the nozzle tip. The receiver (C5R-AN-1A) and the emitter (C5E-ON-1A) were supplied by Automation Direct. If the spray blocked the infrared beam path, the receiver would produce a triggering signal for the PTU board. A complete schematic for this system is shown in Fig. 3.

The same LabView and LaVision systems were used for timing the injection and imaging. Again, a valve actuation signal was sent by the LabView system. Upon sensing the spray at the nozzle tip by the infrared sensor, a trigger signal (corresponding to either the leading or trailing edges of spray) was sent to the LaVision system. The LaVision system then sent two delayed pulses to both the laser and camera for imaging. The delay helped determine droplet sizing at various times during the spray development.

In our experiment, LaVision's DaVis 7.2 Sizemaster program determined the droplet size using the following algorithm. The source images were acquired without smoothing, recommended when high-quality images contain low noise or only a few hot/cold pixels. Then a smooth reference image was created for each source image with equal or more photon counts for all pixels. Subsequently the source image was normalized and inverted by the reference image. The resultant image contained droplets with high-photon-count pixels. Then global segmentation of the image was performed, where areas of the image with a higher than setpoint photon count were chosen for analysis. Then the particle segmentation was performed, finding the average particle diameter for two areas associated with each global segmentation. One area covered a section with a high-photon-count and another area covered a section with the low-photon-count thresholds. Usually a minimum and maximum pixel area are set for the software to avoid detecting noise or very large particles. All parameters set for shadowgraphy are given in Table 3. Droplets that are not in the depth of field may appear faintly with irregular shapes, but their intensity contrast with the background is not high enough so that the global segmentation does not consider them for counting. Figure 4 shows the number distribution N_f for 6 μm diameter calibration microspheres suspended in liquid water. A total of 4135 droplets in 30 images were detected. For this measurement, $d_{10} = 6.4$ μm. As seen, the shadowgraphy technique, like other droplet measurement techniques, tends to "broaden" the distribution with standard deviation $\sigma = 2.2$ μm. As the result of this broadening, the measured d_{32} increases slightly to 8.2 μm.

2.3 Spray Particle Tracking Velocimetry (PTV) Test Setup

The same optical system as in Section 2.2 was used for size dependent particle tracking velocimetry (PVT). A dual-head laser generated two light pulses separated by 10 μs. The LaVision Imager Intense camera was used to grab a double-frame image timed with laser firing. Again, only test 1 flow conditions in Section 2.1 were used.

In our experiment, LaVision's DaVis 7.2 Sizemaster program determined the droplet velocity using the following algorithm. First the sizing algorithm described in Section 2.2 determined the particle size for each frame of the image. The position and size for each particle were stored. The velocity algorithm

TABLE 3: Summary of shadowgraphy and particle tracking velocimetry parameters

Category	Subcategory	Value/Technique
Preprocessing	Image processing	No smoothing
Preprocessing	Reference image	Calculate for each image
Preprocessing	Reference calculation	Strict sliding max. filter
Preprocessing	Filter length	200 pixels
Particle recognition	Reference	Normalize by ref. image
Particle recognition	Global segmentation	40% global threshold
Particle recognition	Particle segmentation	40% low, 60% high
Particle recognition	Particle segmentation	5% AOI expansion
Particle recognition	Particle segmentation	Fill particles
Recognition filter	Maximum low-level area	200% of high-level area
Recognition filter	Minimal area	25 pixels
Velocity parameters	Initial/final window size	$x = 0.5$ mm $\times$ $r = 0.2$ mm
Velocity parameters	Number of passes	1
Velocity parameters	Diameter deviation	15%
Velocity parameters	Initial shift	$x = 0.5$ mm $\times$ $r = 0.0$ mm
Statistical results	Correct depth of field	100 μm reference

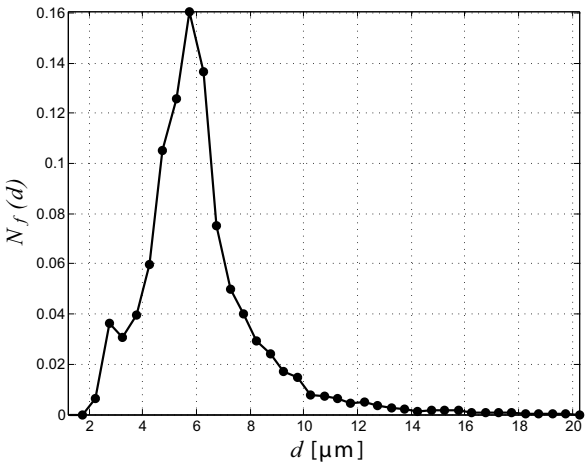

FIG. 4: Number size distribution for 6 μm diameter calibration microspheres measured by the shadowgraphy technique.

identified two pairs of particles with two conditions: the allowed shift and the size. The initial and final window sizes determined the two windows where particles were analyzed in. The initial shift defined the center position of the final window in which particles are accepted relative to each particle location in the initial window. This shift was chosen in the direction of the axial flow of spray so that no reverse motion could be detected. The other parameter determined how much a particle size was allowed to vary between the two windows. All parameters set for PTV are given in Table 3.

2.4 Valve Actuation and Rise Time

To test the valve "actuation" time and flow "rise" time, a pressure transducer was placed in front of the atomizer at a distance of 1 cm along the central

axis. A PCB pressure transducer (model 112A05), a Kistler dual-mode amplifier (model 5004), an iotech wave data logger (model WaveBook/512), and iotech wave recording software (model WaveView7) were used to read and log pressure data. The system sampled 500,000 data points during 50 s with a sampling frequency of 10 kHz. Twenty-five injections were made and the pressure trace was monitored.

The maximum cycle-to-cycle actuation time variability for all twenty-five injections was 8 ms, which justified using the photoelectric sensor. The twenty-five injections resulted in a pressure trace with a standard error (P = 68%) that is plotted in Fig. 5. The rise time t_f for the pressure is a good indicator of time required for liquid/gas flows to reach a maximum value. The rise time is taken as the time required to reach 90% of maximum for a smooth fit to the pressure and is estimated to be 9 ms. The actuation and rise time are shown in Fig. 5.

2.5 Statistical Analalysis

Concentration, d_{32}, volume fraction, number fraction, velocity, and Péclet number are reported using three measurements, each calculated from 100 images. A t distribution is assumed for the data so that $x_{best} = \overline{x} \pm t_{P,\nu}(\sigma_x/\sqrt{N})$ with P = 68%, $N = 3$, $\nu = 2$, and σ_x the standard deviation for the three measurements. The mean values $\overline{x}$, the standard errors $t_{P,\nu}(\sigma_x/\sqrt{N})$, and the curve fitting coefficient of determination R^2 are reported.

2.6 Droplet Size Range for Analysis

To determine the atomization quality, the droplets are analyzed in the range 2–100 μm. For dispersion measurements, however, a smaller range (5–60 μm) is considered. Increasing the minimum droplet size reduces the effect of evaporation as described in Section 1.1. Also, decreasing the maximum droplet size improves the statistics of large droplets, as they occur less frequently in the flow.

3. RESULTS AND DISCUSSION

3.1 Spray Penetration

A total of 200 images were taken for each test described in Section 2.1. The injection (and therefore imaging) was repeated every 2.5 s. The raw images were later processed by a MATLAB code so that the spray axial and radial penetration distances could be determined with ease. First, each image was converted into a binary image, with its pixel value assigned to 1 if the intensity was above a given thresh-

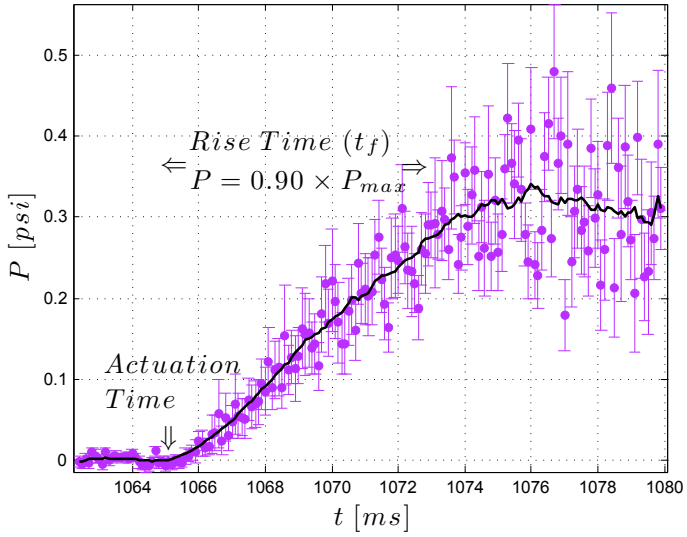

FIG. 5: Pressure rise time at a distance of 1 cm in front of the nozzle due to valve actuation (test 1 flow conditions).

old and 0 if the intensity was below it. Second, the image was filtered for noise (random pixels with high intensity). The spray axial and radial penetration distances were measured by constructing a box around the spray whose length and width represented x and r, respectively. The algorithm for the MATLAB code is provided in Appendix A. The final image was used in the penetration study. Figure 6 shows the raw and filtered binary images obtained by the camera.

Dimensionless axial penetration is plotted versus dimensionless time in Fig. 7. Dimensionless radial penetration is plotted versus dimensionless axial penetration in the same figure. t_f is estimated in Sec-

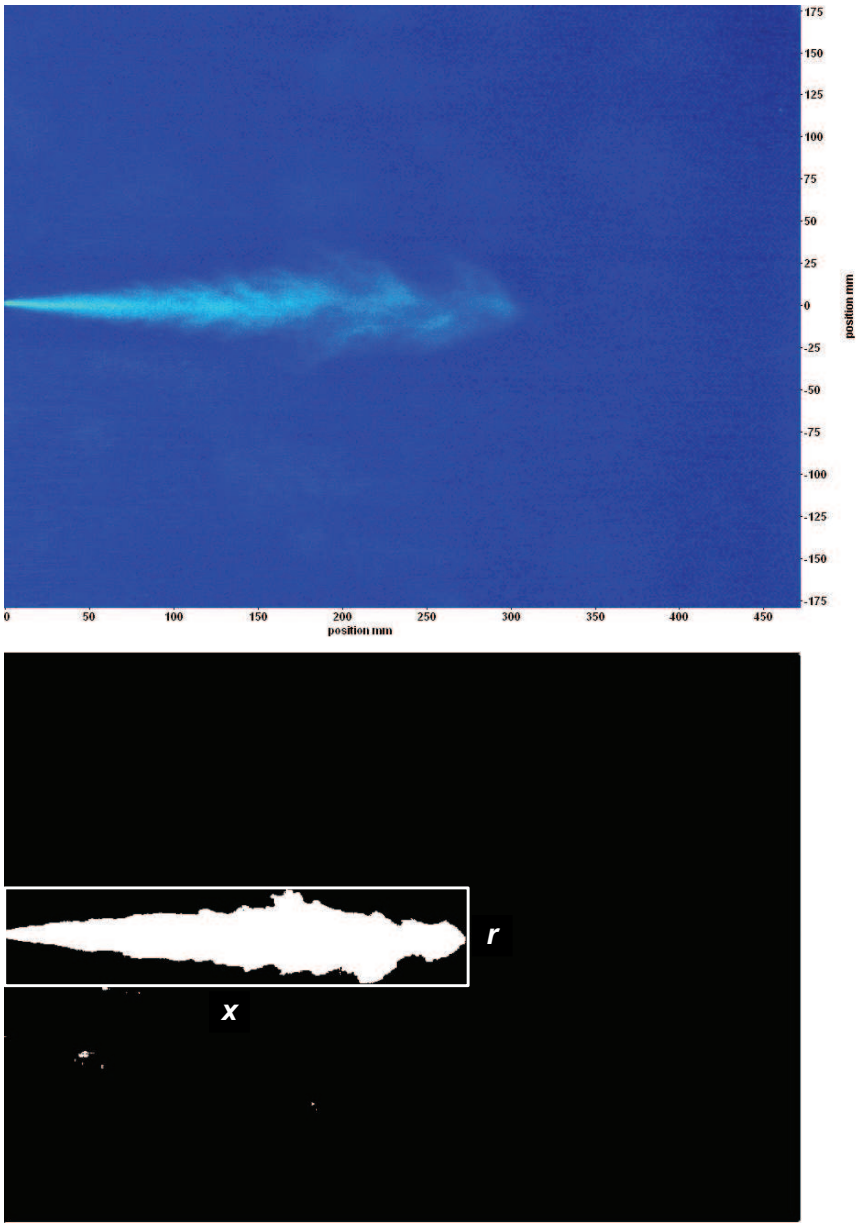

FIG. 6: Spray at t = 24 ms for test 1 raw image (top) and filtered binary image (bottom).

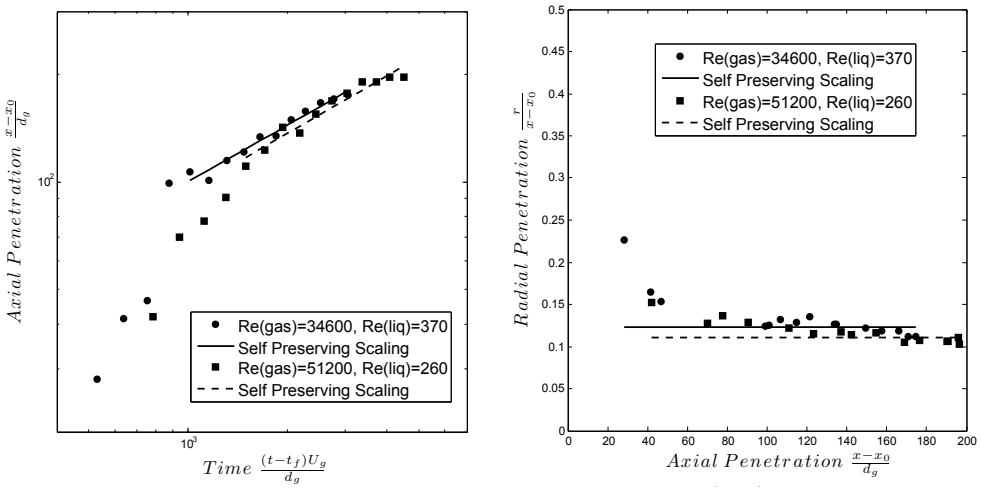

FIG. 7: Dimensionless axial penetration versus dimensionless time (left) and dimensionless radial penetration versus axial penetration (right) (test 1 and 2 flow conditions).

tion 2.4. Two lines on each plot have been fitted to the last 11 data points to describe the self-preserving scaling of the starting jet ($R^2 = 0.99$) according to Eqs. (5) and (6). The virtual origin x_0 is calculated to be –0.005 m. These lines are expected to overlay closely on top of each other. The fitted constants to the self-preserving scaling of the starting jet are provided in Table 4. The constants found are close to those of starting continuous phase jets in the literature.

3.2 Sauter Mean Diameter, Droplet Size, and Concentration Distributions for Steady Spray

The spray was imaged at three axial locations: 50 mm ($x/d_g = 20.7$), 100 mm ($x/d_g = 41.4$), and 200 mm ($x/d_g = 82.9$) away from the nozzle. A radial traverse was performed at each axial location. The radial total concentration is plotted in Fig. 8. As expected, the data collapse on a Gaussian curve ($R^2 = 0.96$). Figure 8 also shows the radial profiles of d_{32} at three different axial locations. d_{32} rises as the spray periphery is approached. These results are in agreement with those found in previous studies (de Vega et al., 2000; Karl et al., 1996; Lasheras et al., 1998) that found that close to the nozzle, larger droplets were more prevalent on the spray periphery.

The correlation of Rizkalla and Lefebvre (1975) predicts $d_{32} = 20.8$ μm for the same atomizer flow conditions, exit diameters, and liquid and gas properties. This value is remarkably close to our experimentally measured value ($d_{32} = 20.8 \pm 0.3$ μm) at

TABLE 4: Summary of self-preserving properties for round turbulent starting jets and transient sprays

Medium	Re_g	n	C_x	C_r
Liquid (Sangras et al., 2002)	3000–12,000	0.5	2.6	0.16
Liquid (Kouros et al., 1993)	53,000	—	—-	0.09–0.10
Liquid (Lahbabi et al., 1993)	2600	0.5	2.9	—
Liquid (Rizk, 1958)	—	—	—	0.13
Gas (Witze, 1983)	2400–9200	0.5	2.5–3.2	—
This study	34,600–51,200	0.5	2.19–2.48	0.10–0.11

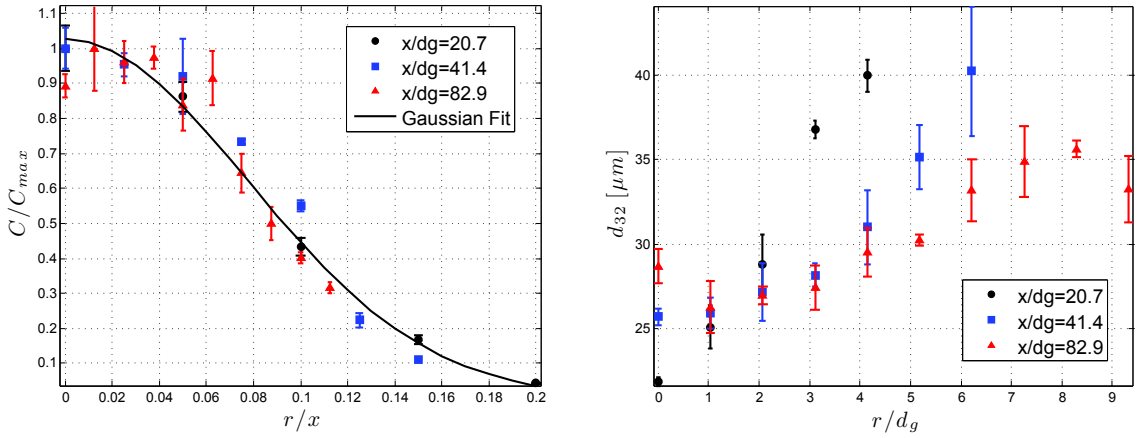

FIG. 8: Total radial concentration of droplets (left) and d_{32} (right) at three different axial distances (test 1 flow conditions).

$x/d_g = 20.7$ for droplet sizes in the range 2–100 μm as described in Section 2.6. This leads to confidence in our measurements.

3.3 Sauter Mean Diameter and Concentration Distribution for Transient Spray

The leading and trailing edges of the spray are shown schematically in Fig. 9. The arrival of the leading edge at a particular location is considered when at least 100 droplets are detected, on average, for the three sets of 100 images taken. Likewise, for the trailing edge there should be at least 100 droplets detected, on average, for the three sets of 100 images taken. The transient behavior of the spray is studied by delaying imaging with respect to the infrared sensor trigger signal. The leading edge of the spray is measured when the infrared beam is blocked (high to low edge trigger), and the trailing edge of the spray is measured when the infrared beam is unblocked (low to high edge trigger).

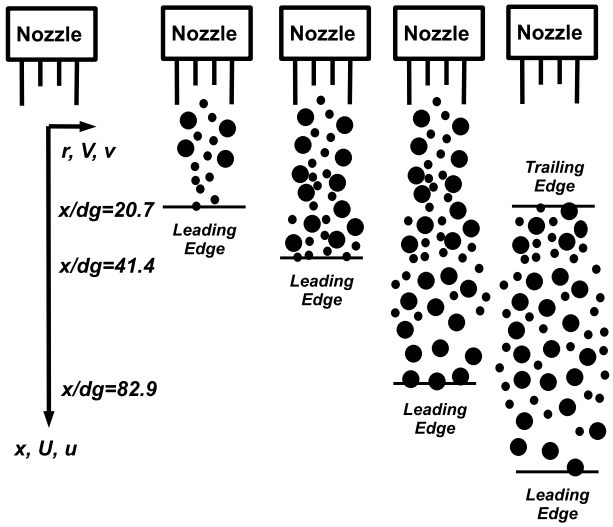

FIG. 9: Schematic for leading and trailing edges of the transient spray.

Figure 10 plots d_{32} and normalized concentration profiles against non-dimensional time delay for the leading and trailing edges at the centerline of spray. At the trailing edge the value of d_{32} is higher at larger axial distances. This can be attributed to two effects. First, small droplets may shrink slightly and leave the measurement droplet size limits due to evaporation at long time delays. Second, the small droplets depart from the centerline more quickly by turbulent dispersion. These two mechanisms can result in higher d_{32} values at the centerline of the spray.

3.4 Droplet Size Distribution for Transient Spray

Figure 11 shows the volume size distributions for the leading and trailing edges at the centerline of the spray with respect to time delay for x/d_g = 20.7, 41.4, and 82.9. The time delay is non-dimensionalized by $t^* = t_d U_g/d_g$.

Figures 10 and 11 show that for x/d_g = 20.7 the leading edge of the transient spray contains more fine droplets than the steady spray. In contrast, the leading edges for x/d_g = 41.4 and 82.9 contain larger droplets so that the volume size distribution is gradually shifted to the right. It is speculated that fine droplets respond to the high flow speed near the nozzle more quickly. In addition, larger droplets originally form closer to the periphery of the spray and do not interact with high flow velocities at the center. As a result, smaller droplets penetrate faster in the axial direction near the nozzle. On the contrary, at larger axial distances (x/d_g = 41.4 and 82.9), larger droplets have gained momentum and penetrate with higher speed in the axial direction. No obvious trend is observed for the trailing edge. It is noted that at

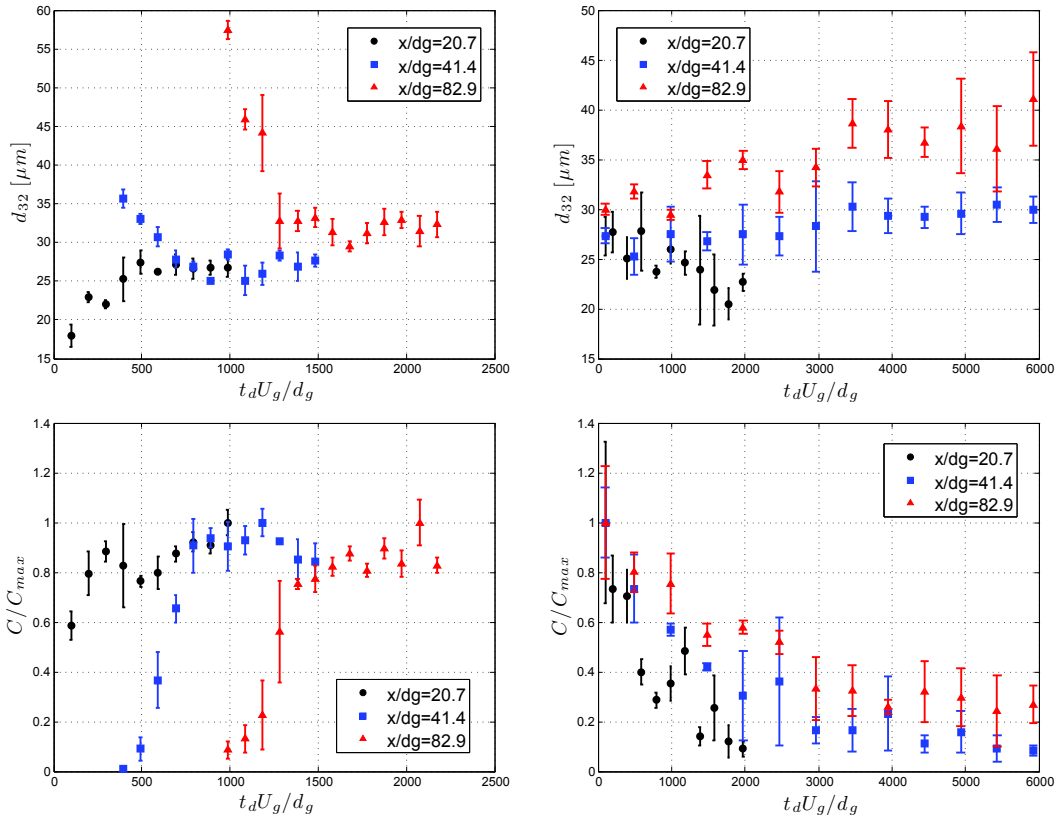

FIG. 10: d_{32} (top) and normalized concentration (bottom) in the leading (left) and trailing (right) edges of the spray (test 1 flow conditions).

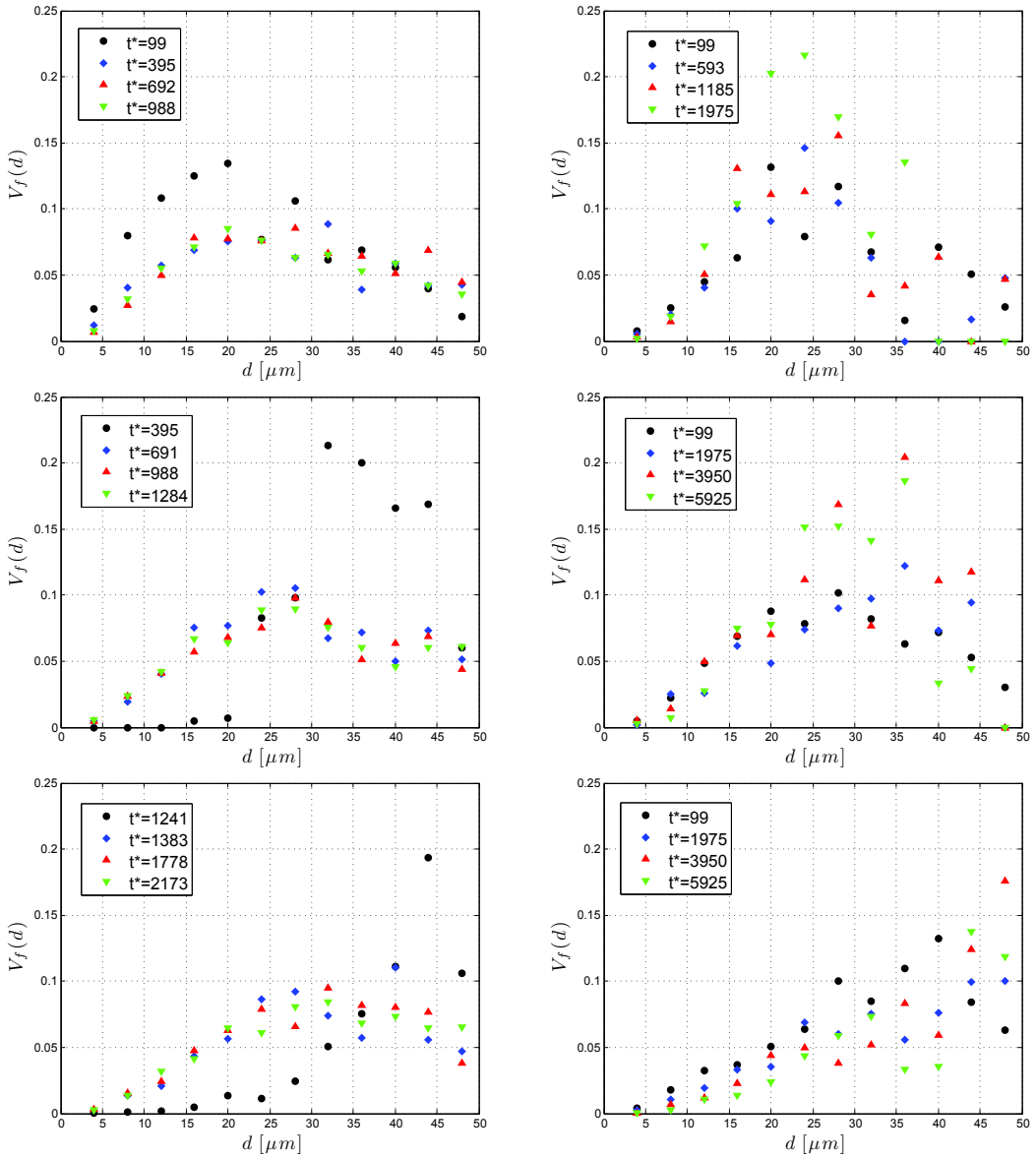

FIG. 11: Volume size distribution on central axis in the leading (left) and trailing (right) edges of the spray at $x/d_g = 20.7$ (top), $x/d_g = 41.4$ (middle) and $x/d_g = 82.9$ (bottom) ($t^* = t_d U_g/d_g$) (test 1 flow conditions).

larger nondimensional time delays the transient spray approaches the steady-state conditions so that the plots reflect any differences.

These results can be better understood considering the mean Stokes number (defined in Table 1). The mean Stokes number for the peak droplet size in the leading edge is calculated as St_m = 5.3, 7.2, and 6.4 for x/d_g = 20.7, 41.4, and 82.9, respectively. For the trailing edge it is calculated as St_m = 7.6, 8.6, and 5.4 accordingly. The mean Stokes number suggests that the relaxation time τ_d for the dominant droplet size in the leading or trailing edges of the spray scales with the mean characteristic time of the flow τ_g at each axial distance of interest. Further research should find

a correlation between τ_d and τ_g with examination of a broader range of axial distances.

3.5 Steady Spray Deceleration

The steady spray deceleration is shown in Fig. 12. The values of B and x_0 in Eq. (2) are found experimentally. B is 6.5, 11.8, 7.4, 5.5, and 5.8 for each droplet size bin from the smallest to the largest bin. Likewise, x_0 is $-131d_g$, $-232d_g$, $-114d_g$, $-63d_g$, and $-57d_g$ for each droplet size bin from smallest to largest bin (R^2 = 0.84, 0.75, 0.68, 0.71, and 0.59). The B values, negative virtual origins, and faster deceleration of smaller droplets in the spray are consistent with results found in the literature (de Vega et al., 2000). The virtual origin decreases as the droplet diameter increases.

3.6 Velocity Distribution for Steady Spray

Figure 13 shows the velocity distribution as a function of radial distance at the axial location of $x/d_g = 41.4$. In particular, profiles of axial velocity U, normalized axial velocity U/U_c, axial fluctuating velocity $\overline{u^2}$, and radial fluctuating velocity $\overline{v^2}$ have been chosen for demonstration. The velocity profiles for other axial locations show a similar trend, and therefore they are not shown for conciseness.

The first trend observed is that larger size bin droplets have higher mean velocities in the axial direction. This is expected since larger droplets have more momentum and are disturbed less by turbulent eddies in the gas phase. Moreover, these velocity profiles are self-similar and appear as Gaussian in the radial direction (Arcoumanis and Gavaises, 1998; de Vega et al., 2000; Hussein et al., 1994; Karl et al., 1996; Kennedy and Moody, 1998; Li et al., 2009).

The fluctuating profiles indicate to what extent particles of a certain size bin follow the turbulent fluctuations in the fluid. Smaller droplets assume higher fluctuating velocities than larger droplets (de Vega et al., 2000; Nijdam et al., 2008). This can be understood in light of turbulent and Kolmogorov Stokes numbers (defined in Table 1). The values of k and ϵ for turbulent and Kolmogorov-Stokes numbers calculations have been approximated by considering the turbulent kinetic energy and dissipation rate on the central axis of gas jets. Figure 14 shows that at all axial distances the values of turbulent and Kolmogorov-Stokes numbers are higher for larger droplets. This means that as droplets become larger, they disperse in a more dissimilar way than the fluid elements since the ratios of droplet relaxation time to turbulent eddy or Kolmogorov characteristic times become higher.

3.7 Péclet Number for Steady Spray

The turbulent dispersion of droplets in the radial direction can be nondimensionalized using droplet dif-

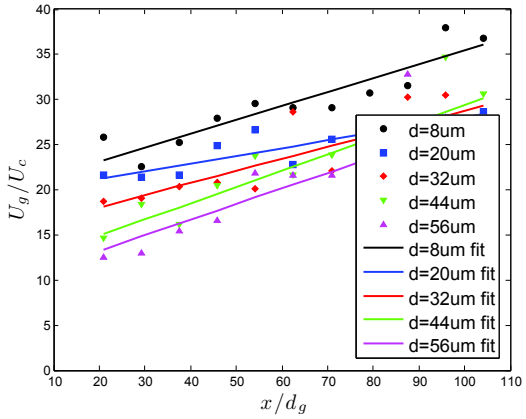

FIG. 12: Steady spray deceleration (test 1 flow conditions).

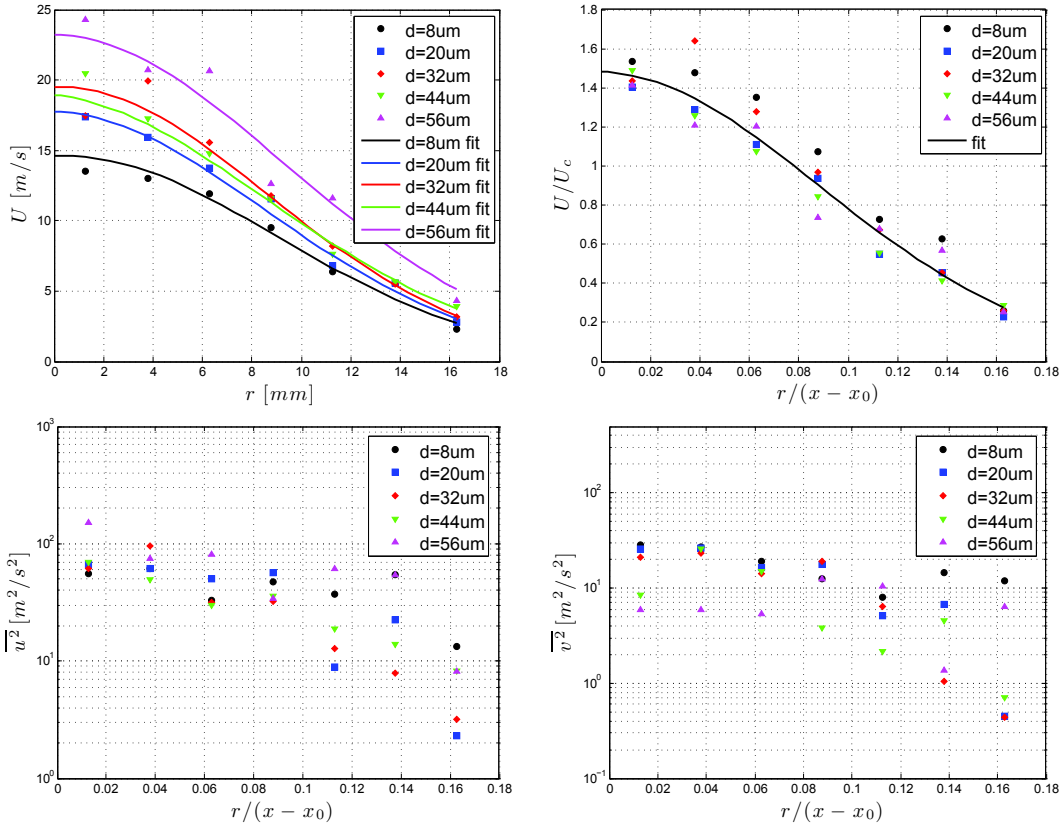

FIG. 13: Axial velocity (top left), normalized axial velocity (top right), axial fluctuating velocity (bottom left), and radial fluctuating velocity (bottom right) for $x/d_g = 41.4$ (test 1 flow conditions).

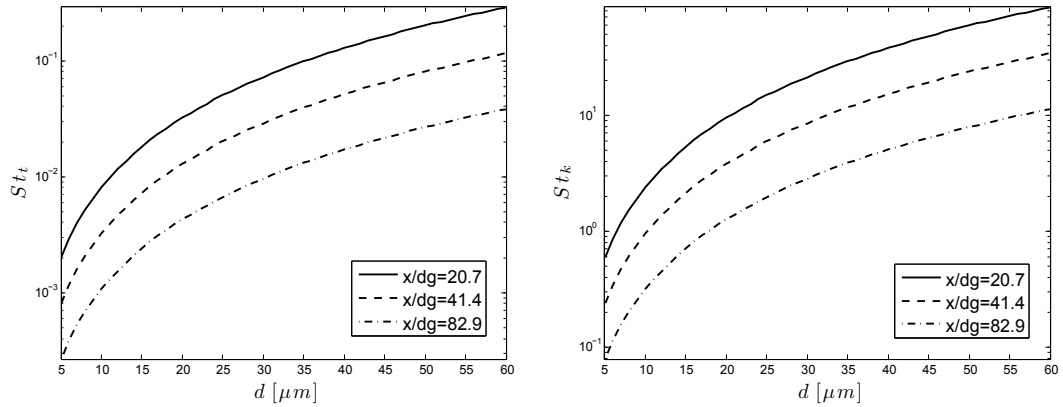

FIG. 14: Turbulent Stokes number (left) and Kolmogorov-Stokes number (right) for axial locations x/d_g = 20.7, 41.4, and 82.9 (test 1 flow conditions).

fusivity and the Lagrangian Péclet number in Eqs. (3) and (4). Since the droplet response to turbulence is more predictable at larger distances from the nozzle, the average Péclet number is calculated from

$x/d_g = 41.4$ to $x/d_g = 82.9$. Figure 15 shows the Péclet number as a function of droplet size. Larger droplets show a higher Péclet number than smaller droplets. This confirms the hypothesis in Section 3.6 that smaller droplets disperse more effectively in the radial direction due to turbulent fluctuations (Kennedy and Moody, 1998).

3.8 Velocity Distribution for Transient Spray

Figure 16 shows the velocity distribution as a function of time delay at the axial location of $x/d_g = 41.4$ on the centerline of the spray. In particular, profiles of axial velocity U, axial fluctuating velocity $\overline{u^2}$, and radial fluctuating velocity $\overline{v^2}$ have been chosen for demonstration. Again, the data have been plotted on the same scale as for the steady spray (Fig. 13) so that the relative magnitude of the quantities of interest could be compared. For conciseness, the results for other axial locations are not shown but are similar.

For the leading edge the mean axial velocity for larger droplets is higher than that of smaller droplets. The magnitude of this velocity does not change notably as a function of time delay. The velocity magnitude is also similar to those observed for steady sprays. The unchanging value of this velocity as a function of time delay in the leading edge shows similarity between continuous phase starting jets and transient sprays. As one would anticipate, the magnitude of the axial velocity at the trailing edge is smaller compared to the leading edge. This magnitude is similar for all droplet sizes, and it declines slowly for larger time delays.

At the leading edge the magnitude of axial and radial fluctuating velocities are about the same as the equivalent steady case. Again, small droplets move with higher fluctuating velocities than large droplets. For the trailing edge, these velocities drop an order of magnitude and no correlation can be observed between velocity and droplet size. The velocity data is rather very scattered. It is speculated that the magnitude of turbulent and Kolmogorov-Stokes numbers drops quickly when the injection momentum is cut. As a result, all droplets track fluid turbulent motion more easily. In this region the flow reaches very low Reynolds numbers, where all droplets follow the random fluid motion with the same likelihood.

4. CONCLUSIONS

Steady and transient droplet dispersion characteristics of an air-assist internally mixing cone spray have been studied using imaging, shadowgraphy, and particle tracking velocimetry (PTV). While

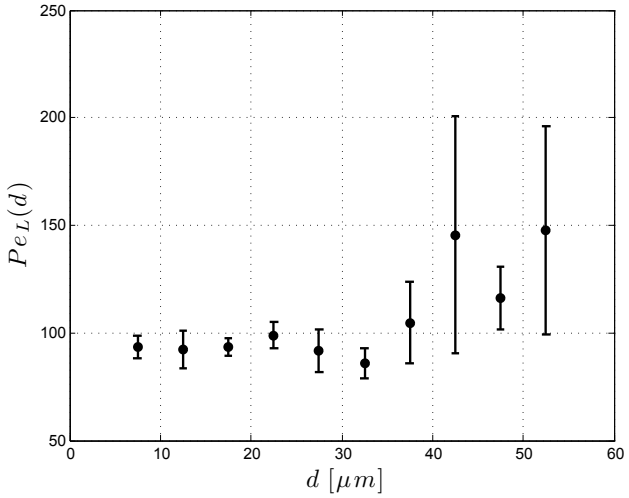

FIG. 15: Average Péclet number from $x/d_g = 41.4$ to $x/d_g = 82.9$ (test 1 flow conditions).

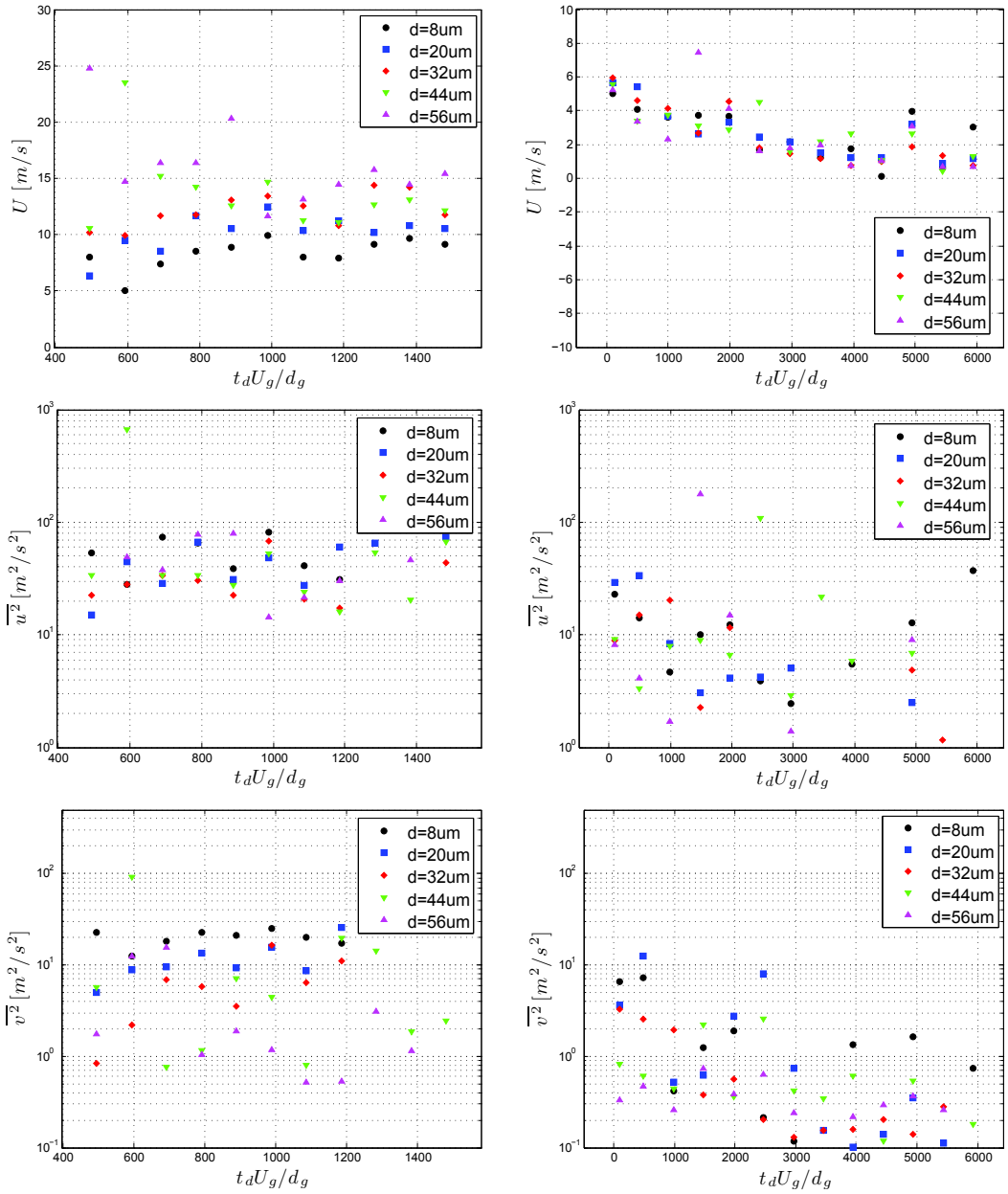

FIG. 16: Axial velocity (top), axial fluctuating velocity (middle), and radial fluctuating velocity (bottom) for leading (left) and trailing (right) edges of the transient spray at $x/d_g = 41.4$ (test 1 flow conditions).

some results confirm previous studies, others are novel. The following conclusions may apply to many dilute sprays at far enough distances from the breakup regime, where flow patterns are self-similar.

4.1 Summary of Confirmed Results in the Literature

For steady operation, the spray quality ($d_{32} = 20.8 \pm 0.3$ μm) satisfies accepted Sauter mean diameter

correlations that relate d_{32} to fluid properties and flow conditions. Total concentration profiles are distributed in a Gaussian shape when plotted versus radial distance from the central axis. Furthermore, concentration profiles are self-similar so that they all collapse on the same curve when plotted versus nondimensional radial distance. The mean axial velocity profiles also appear to be Gaussian as a function of radial distance.

For the steady operation, spatial variation of atomization quality reveals that larger droplets form closer to the periphery of the spray while smaller droplets form close to the central axis. The velocimetry and Péclet number analyses confirm that smaller droplets migrate to the periphery of the spray faster ($\mathrm{Pe}_L(d = 7.5\ \mu\mathrm{m}) = 93.3$) than larger droplets ($\mathrm{Pe}_L(d = 52.5\ \mu\mathrm{m}) = 147.7$) due to turbulent dispersion. The deceleration plot and the mean axial velocity profiles indicate that larger droplets move faster than smaller ones in the axial direction.

4.2 Summary of Novel Results

Transient spray penetration test results reveal that the overall spray axial and radial dispersion is self-similar ($C_x = 2.19 - 2.48$, $C_r = 0.10 - 0.11$, and $n = 0.5$) after a certain nondimensional time and axial distance. In the self-similar region, the spray behaves like a gas jet since the smallest droplets in the spray disperse like fluid elements in the gas background.

The droplet volume fraction for the leading edge peaks at 20 μm, 33 μm, and 44 μm for x/d_g of 20.7, 41.4, and 82.9, respectively. In the trailing edge, droplet volume fraction peaks at 24 μm, 36 μm, and 42 μm for the same nondimensional axial distances. Likewise, d_{32} varies in the leading edge as a function of time delay and axial distance. This variation for the trailing edges is less pronounced. The mean Stokes number analysis suggests that the relaxation time τ_d for dominant droplet size in the leading and trailing edges of the spray is correlated with the mean characteristic time of the flow τ_g at the axial distances examined. For the leading edge the mean Stokes number is calculated as St_m = 5.3, 7.2, and 6.4 and for the trailing edge it is calculated as St_m = 7.6, 8.6, and 5.4 for the same axial distances, respectively. Future research must find this correlation in a broader range for all axial distances within the spray.

PTV of the transient spray in the leading edge reveals similar mean and fluctuating velocities to the steady spray. Large droplets have high mean axial velocities while small droplets have higher fluctuating radial velocities. These velocities do not change appreciably as a function of time delay. The mean and fluctuating velocities for the trailing edge, however, are an order of magnitude (factor of 10) less than those for steady spray. These velocities decrease as a function of time delay. The mean axial and fluctuating radial velocities have equal magnitudes for all droplet sizes. The trailing edge of the spray exhibits low-Reynolds-number and large-eddy flow conditions with lower turbulent and Kolmogorov-Stokes numbers. Such flows tend to move droplets, whether large or small, with the same likelihood as fluid elements.

ACKNOWLEDGMENTS

The authors acknowledge the Natural Sciences and Engineering Research Council of Canada (NSERC) and Stantec Consulting, Ltd., for financial support. The authors also thank Ehsan Faghani for helping with pressure testing of the atomizer.

REFERENCES

Arcoumanis, C. and Gavaises, M., Linking nozzle flow with spray characteristics in a diesel fuel injection system, *Atomization Sprays*, vol. **8**, pp. 307–347, 1998.

de Vega, M., Rodríguez, P., and Lecuona, A., Mean structure and droplet behavior in a coaxial airblast atomized spray: Self-similarity and velocity decay functions, *Atomization Sprays*, vol. **10**, pp. 603–626, 2000.

Engelbert, C., Hardalupas, Y., and Whitelaw, J. H., Breakup phenomena in coaxial airblast atomizers, *Proc. R. Soc. Lond. A*, vol. **451**, pp. 189–229, 1995.

Eroglu, H. and Chigier, N., Initial drop size and velocity distributions for airblast coaxial atomizers, *J. Fluids Eng.*, vol. **113**, pp. 453–459, 1991.

Hardalupas, Y., Taylor, A. M. K. P., and Whitelaw, J. H., Velocity and particle-flux characteristics of turbulent particle-laden jets, *Proc. R. Soc. London, Ser. A.*, vol. **426**, pp. 31–78, 1989.

Hardalupas, Y. and Whitelaw, J. H., Characteristics of sprays produced by coaxial airblast atomizers, *J. Propul. Power*, vol. **10**, no. 4, pp. 453–459, 1994.

Hussein, H. J., Capp, S. P., and George, W. K., Velocity measurements in a high-reynolds-number, momentum-conserving, axisymmetric, turbulent jet, *J. Fluid Mech.*, vol. **258**, pp. 31–75, 1994.

Karl, J. J., Huilier, D., and Henri, B., Mean behavior of a coaxial air-blast atomized spray in a co-flowing air stream, *Atomization Sprays*, vol. **6**, pp. 409–433, 1996.

Kennedy, I. M. and Moody, M. H., Particle dispersion in a turbulent round jet, *Exp. Therm. Fluid Sci.*, vol. **18**, pp. 11–26, 1998.

Kouros, H., Medina, R., and Johari, H., Spreading rate of an unsteady turbulent jet, *AIAA J.*, vol. **31**, pp. 1524–1526, 1993.

Lahbabi, F. Z., Botee, J., Nuglisch, H. J., and Charnay, G., Analysis of starting and steady turbulent jets by image processing techniques, Experimental and numerical flow visualization, *ASME Fluids Eng. Division*, vol. **172**, pp. 315–321, 1993.

Lasheras, J. C., Villermaux, E., and Hopfinger, E. J., Break-up and atomization of a round water jet by a high-speed annular air jet, *J. Fluid Mech.*, vol. **357**, pp. 351–379, 1998.

Li, L. K. B., Dressler, D. M., Green, S. I., and Davy, M. H., Experiments on air-blast atomization of viscoelastic liquids, Part 1: Quiescent conditions, *Atomization Sprays*, vol. **19**, no. 2, pp. 1–34, 2009.

Morawska, L., Droplet fate in indoor environments, or can we prevent the spread of infection?, *Indoor Air*, vol. **16**, pp. 335–347, 2006.

Nijdam, J. J., Langrish, T. A. G., and Fletcher, D. F., Assessment of an Eulerian CFD model for prediction of dilute droplet dispersion in a turbulent jet, *Appl. Math. Model.*, vol. **32**, pp. 2686–2705, 2008.

Rizk, N. K. and Lefebvre, A. H., Spray characteristics of plain-jet airblast atomizers, *Trans. ASME J. Eng. Gas Turbines Power*, vol. **106**, pp. 639–644, 1984.

Rizk, W., Experimental studies of the mixing process and flow configurations in two-cycle engine scavenging, *Proc. Ins. Mech. Eng., IMechE*, vol. **172**, pp. 417–424, 1958.

Rizkalla, A. and Lefebvre, A. H., The influence of air and liquid properties on air blast atomization, *ASME J. Fluids Eng.*, vol. **97**, no. 3, pp. 316–320, 1975.

Sakai, T., Kito, M., Saito, M., and Kanbe, T., Characteristics of internal mixing twin-fluid atomizer, *Proc. 3rd Int. Conf. Liquid Atomization and Sprays*, pp. 235–241, 1978.

Sangras, R., Kwon, O. C., and Faeth, G. M., Self-preserving properties of unsteady round nonbuoyant turbulent starting jets and puffs in still fluids, *J. Heat Transfer*, vol. **124**, no. 3, pp. 460–469, 2002.

Shi, H. and Kleinstreuer, C., Simulation and analysis of high-speed droplet spray dynamics, *J. Fluids Eng.*, vol. **129**, pp. 621–633, 2007.

Varga, C. M., Lasheras, J. C., and Hopfinger, E. J., Initial breakup of a small-diameter liquid jet by a high-speed gas stream, *J. Fluid Mech.*, vol. **497**, pp. 405–434, 2003.

Wells, M. R. and Stock, D. E., The effects of crossing trajectories on the dispersion of particles in a turbulent flow, *J. Fluid Mech.*, vol. **136**, p. 31, 1983.

Witze, P. O., Hot-film anemometer measurements in a starting turbulent jet, *AIAA J.*, vol. **21**, pp. 308–309, 1983.

APPENDIX A. MATLAB ALGORITHM FOR IMAGE PROCESSING

- Set the image intensity threshold to 0.2.
- Set the noise removal constant to 5.
- Define the number of pixels in the image per unit length.
- Read 10 images for each time delay in MATLAB using the $imread()$ command.
- Convert the images to the binary format using the image intensity threshold and the $im2bw()$ command. Any pixel with an intensity greater than threshold will be assigned an intensity of 1 or otherwise an intensity of 0.
- Filter the binary images for noise using the noise removal constant and the $medfilt2()$ command. This command performs median filtering of an

image matrix in two dimensions. Each output pixel contains the median value in a neighborhood around the corresponding pixel which is as large as the noise removal constant in length.

- Visually inspect the 10 pictures and crop the spray, which appears as a white region, using the $imcrop$ command in each image. This command allows the user to draw a box around the edges of the spray and to store the box width and length in memory in pixels.
- Convert the box dimensions from pixels to meters.
- Calculate the mean and standard deviation for the box dimensions using the data for the 10 images for the same time delay.